WILEY | Hindawi

Research Article

Experimental and Finite Element Study on 7A04 Aluminum Alloy Tube Confined High Strength Concrete Long Column

Zuo-Jin Zhang ⓘ,[1] **Feng-Xia Han ⓘ,**[1,2] **and Qing Liu ⓘ**[1,2]

[1]*School of Civil Engineering and Architecture, Xinjiang University, Urumqi 830047, China*
[2]*Xinjiang Key Lab of Building Structure and Earthquake Resistance, Urumqi 830047, China*

Correspondence should be addressed to Feng-Xia Han; fxhan@xju.edu.cn

7A04 aluminum alloy has high strength and strong corrosion resistance, and its quality is only 1/3 of steel. Using 7A04 aluminum alloy to replace ordinary steel tube to confined concrete, it can effectively reduce the member section, reduce the weight of the structure, and more in line with the material requirements of large span materials and high-rise buildings. In this paper, nine groups of 7A04 aluminum alloy tube confined high strength concrete long column were tested under axial compression and eccentric compression with aspect ratio and eccentricity as variables. And the corresponding ABAQUS finite element model was established. The results show that the failure phenomena of the nine groups are basically the same, and the specimen deflection curve shape is similar to the sine half-wave curve. The ultimate bearing capacity of the specimen decreases with the increase of aspect ratio and eccentricity. When the axial compression or eccentricity of the specimen is small, the variation of the longitudinal and transverse strain at the midspan is similar in the elastic stage. When the eccentricity is large, the longitudinal and transverse strain at the midspan of the specimen is obviously tensile at one side and compressive at one side at the beginning. Finally, based on the test and simulation results, a formula for calculating the bearing capacity of 7A04 aluminum alloy tube high strength concrete long columns is proposed. This formula can better predict the stable bearing capacity of the specimen, which has certain reference significance for the structural design of 7A04 aluminum alloy tube high strength concrete long columns.

1. Introduction

Tube confined concrete composite structure has good ductility, high strength, and simple construction [1]. And compared with traditional building materials, it has good impact resistance [2–4]. On the one hand, steel tube confined concrete can restrict the development of concrete cracks and restrict the transverse expansion of concrete; on the other hand, concrete can limit the inward buckling of steel tubes, and the utilization of materials can be maximized by the mutual restriction of the two materials. At present, the research on steel tube confined concrete column by experts and scholars in China and abroad has been relatively mature, and the stress mechanism of steel tube confined concrete components has been basically grasped [5–9]. However, there are relatively few studies on the components of aluminum alloy tube concrete.

Compared with ordinary structural steel, aluminum alloy has the advantages of light weight, strong corrosion resistance, and beautiful appearance. Compared to other materials [10–13], aluminum alloy is a typical environmentally friendly green building material. Aluminum alloy has attracted more and more attention from civil engineering practitioners for its excellent performance, compared with other materials. Although aluminum alloy is expensive, it has become the most widely used metal building material except steel due to its many advantages. As early as the 1930s, Templin et al. [14] have studied the compression performance of aluminum alloy members. Subsequently, Holt, Clark and Rolf, and Hill [15–17] explored the mechanical properties of aluminum alloy compression-bending members and proposed the corresponding bearing capacity calculation formula. In 1970, Faella and Mazzolani and Valtinat and Muller [18, 19] studied the stability coefficient of

aluminum alloy axial compression confined concrete columns by numerical analysis and experiment. The results show that the bearing capacity of the specimen decreases gradually with the increase of aspect ratio. Subsequently, Frey and Mazzolani [20, 21] conducted compression-bending tests on aluminum alloy columns with various cross-sections and found that the stability performance of specimens affected by defects decreased with the increase of aspect ratio. The domestic research on aluminum alloy components started late. Since 2000, many domestic scholars [22–25] have carried out the research on aluminum alloy components. A large number of aluminum alloy building construction studies have been reported since 2007 promulgated the first "Aluminum Structure Design Specification" [26] in China.

Compared with steel components, aluminum alloy also shows excellent working performance in strong acid and alkaline environment [27]. The use of high strength aluminum alloys instead of ordinary steel tubes filled with concrete can not only effectively improve the overall mechanical performance of the components and reduce the weight of the structure but also save a lot of financial and material resources for the later maintenance of steel components. At present, most of the researches on tube confined concrete columns at home and abroad focus on steel tube confined concrete components, and a small amount of aluminum tubular tube confined concrete is only limited to the 5 series and 6 series aluminum alloy, and most of them are short columns. Considering the obvious differences in the physical properties of steel tubes and aluminum alloys, it is necessary to conduct further research on long column members filled with concrete in 7A04 aluminum alloy tubes.

In this paper, the axial compression and eccentric compression tests of 9 groups of 7A04 aluminum alloy long column specimens were carried out, and the aspect ratio and eccentricity were used as variables to explore their influence on the mechanical properties of 7A04 aluminum alloy tube confined concert long column. Finally, based on the finite element numerical analysis and experimental results, a formula for calculating the bearing capacity of long column specimens is proposed.

2. Experimental Program

2.1. Design of Specimen. In order to explore the influence of aspect ratio and eccentricity on the mechanical properties of 7A04 aluminum alloy tube high strength concrete long columns, as shown in Table 1, nine groups of specimens are designed according to GB 50936-2014 "TECHNICAL SPECIFICATION for CONCRETE FIllED STEEL TUBULAR STRUCTURES" [28]. Add a group of short columns with the same section size as the control group. To avoid the specimen height that is too small, end effect is obvious; at the same time, in order to avoid the specimen height that is too high, the specimen buckling failure occurs. The specimen height is designed to be 400 mm, the outer diameter of the section is 100 mm, and the aspect ratio is 4. Unwelded pads at both ends of specimens, before the formal experiment, the end of the short column specimen and the long

column specimen was polished flat. Incidentally, the three specimens were arranged in parallel to take into account the discreteness of the specimens in each set of tests.

The concrete strength grade of the samples is C60, and the wall thickness of each 7A04 series aluminum alloy tube is 3 mm. The material, pouring method, mix ratio, and curing condition (curing for 28 days at room temperature) of all the samples are controlled the same, and only aspect ratio and eccentricity are taken as the variables of the study.

The basic mechanical properties of the materials are shown in Tables 2 and 3.

2.2. Loading and Measuring System. The samples were tested in the YJW10000 microcomputer controlled hydraulic servo press in the Key Laboratory of Earthquake Resistance of Xinjiang University according to GB/T 50152-2012 "Standard for Test Methods of Concrete Structures" [29]. The load is loaded by displacement control at a rate of 1 mm/min. When the load drops to about 70% or the deformation is large enough, the load stops, and the specimen is considered damaged. For the eccentric compression confined concrete column, the external bolt rod is jacked at both ends of the member to prevent lateral sliding of the member in the loading process. Both ends of the short column sample are constrained by the fixed end; a knife hinge bracket is provided at both ends of the long column specimen. The sample is hinged at both ends in the *X* direction and fixed at both ends in the *Y* direction. The hinge bracket is shown in Figure 1.

The vertical displacement as well as the transverse and longitudinal strains of the specimen was recorded continuously. The displacement gauge was arranged parallel to the height of the specimen to measure the overall vertical displacement, and the concentricity of the axial load was verified at the initial loading stage. Flexural instability failure of a component may occur due to accidental errors during fabrication and installation when the aspect ratio of the component is too large. Therefore, the horizontal displacement is measured and recorded to analyze the deflection of the midspan under pressure by means of a displacement meter placed in the midspan. Deflection values at both ends of the column are obtained by displacement gauges set at L/4 and 3L/4 of the column. Considering that the middle of the column span is the most dangerous section of the column, a set of transverse and longitudinal strain gauges which are perpendicular to each other are pasted to measure the variation of transverse deformation coefficient at the middle of the column dangerous section when the member is loaded. Similarly, a set of transverse and longitudinal strain gauges, which are perpendicular to each other, are also attached to the L/4 and 3L/4 positions of the column to monitor end deformation. The schematic diagram of strain gauge arrangement and column loading is shown in Figure 2.

3. Results and Analysis

3.1. Failure Modes and Characteristics. Figure 3 is the typical failure mode of the specimen. The short column is the central swelling failure. The failure mode of 8 7A04 aluminum

TABLE 1: Basic parameter table of specimen.

Specimen label	Diameter, D (mm)	Thickness, t (mm)	f_{cu}, (MPa)	Eccentricity, e (mm)	Column height, L (mm)	Aspect ratio, L/D (mm)
AHCSE0-1	100	3	60.6	0	1600	16
AHCSE15-1	100	3	60.6	15	1600	16
AHCSE30-1	100	3	60.6	30	1600	16
AHCSE0-2	100	3	60.6	0	1300	13
AHCSE15-2	100	3	60.6	15	1300	13
AHCSE30-2	100	3	60.6	30	1300	13
AHCSE0-3	100	3	60.6	0	1000	10
AHCSE15-3	100	3	60.6	15	1000	10
AHCSE30-3	100	3	60.6	30	1000	10
AHCSE0	100	3	60.6	0	400	4

*In "AHCST (χ)," "AHCS" represents the aluminum alloy tube high strength concrete column, D is specimen diameter, and L is specimen height. "$e\,(\chi)$" is the eccentricity distance of the specimen, and f_{cu} is the cube compressive strength of concrete.

TABLE 2: 7A04 aluminum alloy chemical composition.

Chemical composition	Si	Fe	Cu	Mn	Mg	Cr	Zn	Ti	Al	Other
Mass fraction (%)	0.22	0.25	1.41	0.21	1.85	0.18	5.01	0.02	90.79	0.06

TABLE 3: Material properties of aluminum alloy.

Thickness (mm)	$f_{0.2}$ (MPa)	Tensile strength (MPa)	Poisson's ratio v	Elasticity modulus, E (MPa)
3	400	470	0.3	71000

*$f_{0.2}$ is the yield strength of aluminum alloy.

alloy tube high strength concrete long columns under eccentric compression and axial compression test is the same, and all of them show bending failure at the middle part of the span. Among them, one specimen was staggered between the hinge support and the end of the specimen due to the uneven loading of the end concrete, and there was end failure.

As concrete limits the inward buckling of aluminum tubes, there is no obvious change in the surface of aluminum alloy before the peak load during the short column loading. When the load reaches the peak point, there is a slight outward bulge in the middle of the specimen, and the bulge is further intensified after the peak point, and the aluminum tube has yielded. As the displacement continues to increase, the load borne by the specimen continues to decrease, and the load-displacement curve of the specimen does not show an obvious plastic stage. At this time, small cracks can be observed on the surface of the aluminum tube under continuous loading. This shows that the plasticity of 7A04 high strength aluminum alloy is weakened while the strength is improved.

The failure mode and failure phenomenon of long column specimens under axial compression and eccentric compression are basically the same, which are all bending failures at the middle part of the span. The final deformation shape of the specimen is similar to the sine half-wave curve.

There was no significant change in the surface of the specimen at the initial loading stage of the axial compression test, and slight deflection deformation of the specimen could be observed when the load approached or reached the peak value. When a load of the eccentric compression specimen reaches about 70% of the peak load, obvious deflection deformation has been observed in the middle part of the specimen. The concrete at the end of the specimen after unloading is about 0.5-1 mm higher than that of the aluminum alloy tube wall, which is due to the elastic rebound of the aluminum alloy tube after loading.

At the initial stage of loading, the specimen is in the elastic stage. At this time, the load and displacement are linear, and the appearance of the specimen is basically unchanged. Occasionally hear the "Zizi" sound when concrete produces microcracks. At this time, the overall appearance of the specimen changed little, and the increment of the strain gauge and the displacement meter reading was relatively slow. When the specimen reaches the elastic-plastic stage, the axial force ratio between the aluminum alloy tube and the core concrete changes continuously, the cracks in the concrete expand, and the specimen makes a "crackle" sound. At this time, the specimen shows obvious deflection deformation at the middle part of the span, and the increment of strain gauge and displacement meter reading begins to accelerate. After the peak point, the specimen entered the softening stage. At this time, the load of the specimen decreased sharply with the increase of displacement, and the midspan deflection deformation also increased. The displacement meter reading increased rapidly, and most of the strain gauges in the midspan overflowed, and the test was stopped.

3.2. Load-Displacement Curves. Figure 4 shows the axial load-displacement curve of the test. According to the

(a)   (b)
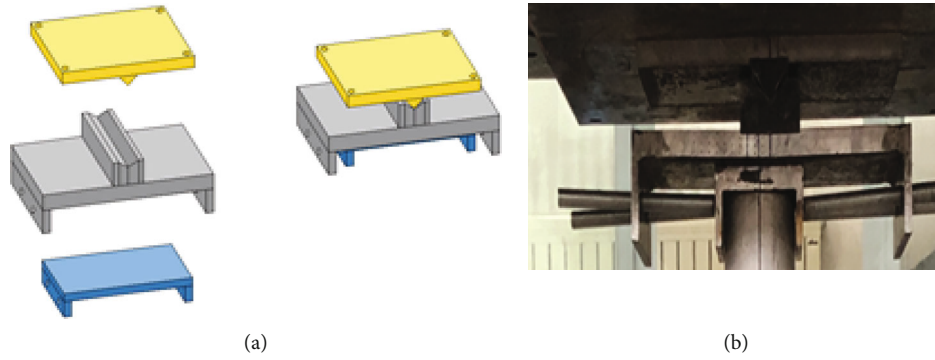
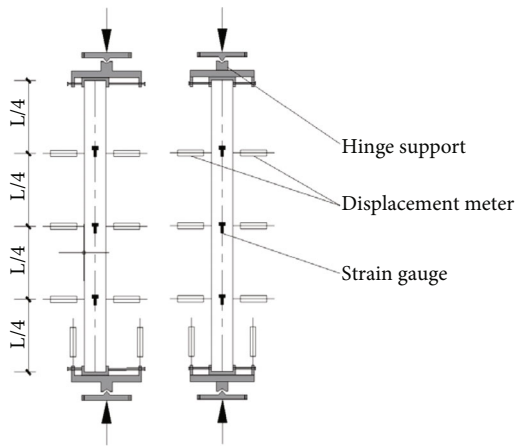FIGURE 1: (a) Hinge support. (b) Hinge support.

FIGURE 2: Schematic diagram of strain gauge arrangement and column loading.

different stiffness of the curve, it can be roughly divided into three stages, namely, elastic stage, elastic-plastic stage, and softening stage.

The slope of the axially loaded specimen is large, and the elastic critical point of the specimen (the elastic critical point is the intersection of the specimen from the elastic stage to the elastic-plastic stage) is about 77%-85% of the ultimate load. In the elastic-plastic stage, the midspan part of the specimen produced slight deflection deformation. As the load of specimens increases slowly, the curve gradually changes from straight line to curve. And about the load continues to increase, the deflection deformation becomes more and more obvious in the midspan part of the specimen. After the peak point, the specimen enters the softening stage. At this time, the aluminum alloy in the midspan yielded, and the load increased by concrete was much smaller than that decreased by aluminum tube. Due to the existence of the second-order effect, the load of the specimen decreased continuously. The larger the aspect ratio of the specimen was, the faster the bearing capacity of the specimen decreased.

The stiffness of the specimen under eccentric compression is small, and the elastic critical force is about 70%–82% of the peak load. The slope of the specimen decreases in plastic stage, and the upward trend of the curve tends to be gentle. In the softening stage, the larger the eccentricity of the specimen is, the slower the stiffness degradation of

the specimen is, and the slower the load curve decreases. The increase of eccentricity reduces the stiffness and bearing capacity, but the ductility increases.

It is worth noting that in this experiment, for axially compressed specimens, the larger the aspect ratio of the specimen is, the faster the load decreases during the softening stage. This may be because the component with large aspect ratio is more sensitive to the influence of defects, and the bending stiffness of the specimen is small. Therefore, the slope of the specimen with large aspect ratio is not only low in the elastic stage but also the decline rate is faster in the softening stage.

3.3. Load-Deflection Curve. As can be seen from Figure 5, the development law of load-deflection curves of nine groups of long column specimens is roughly the same. This paper will analyze from the following aspects.

For the rise section of the curve, the midspan deflection of the axial compression member developed slightly and increased slowly at the initial loading stage, and the load and deflection curves showed a linear relationship, which also indicated that the 7A04 aluminum alloy filled concrete specimen had good bending stiffness. With the increase of length-diameter ratio, the stiffness of the specimen decreases gradually. At this time, the specimen is subjected to full-section compression along the length direction. At this time, the force of aluminum tube is greater than that of concrete, and the aluminum tube and internal concrete are in a state of separate force. The elastic proportional limit of axially loaded specimens is approximately 77%–85% of the ultimate load.

The larger the eccentricity of the eccentric compression member specimen is, the faster the specimen deflection develops. At the beginning of loading, the midspan part of eccentric compression specimen shows obvious compression and tension at one end. When the eccentricity is 15 mm, the elastic critical force of the specimen is 75%-82% of the ultimate load, and when the eccentricity is 30 mm, the elastic critical force of the specimen is 70%-80% of the ultimate load.

For curve descending section, when the load of axial compression member reaches the peak point, the midspan part has produced obvious deflection deformation. The additional bending moment caused by the second-order effect cannot be ignored. With the increase of deflection,
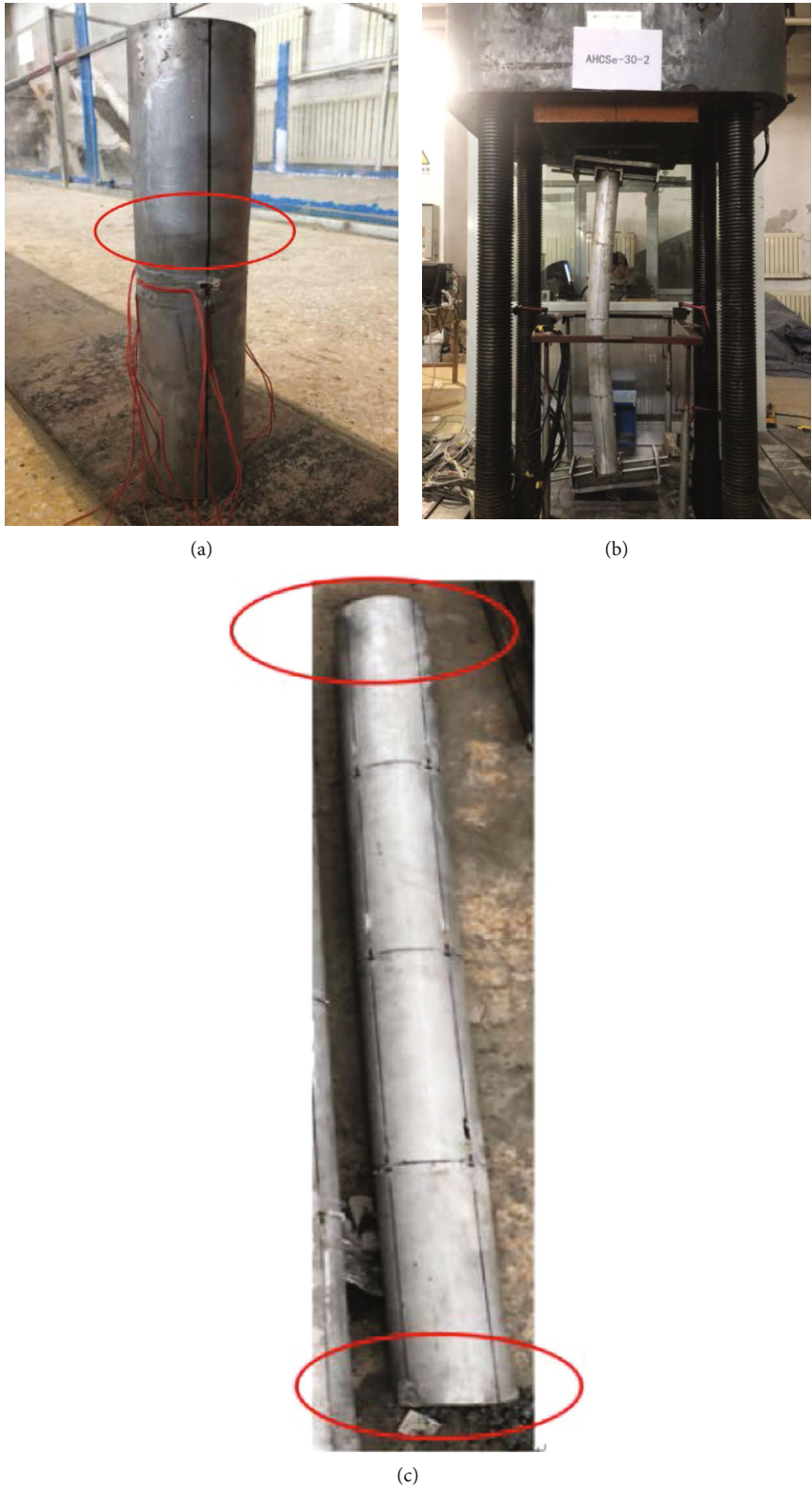
(a)

(b)

(c)

Figure 3: Failure pattern of aluminum alloy concrete columns: (a) central swelling failure; (b) midspan bend; (c) end failure.

the additional bending moment increases, and the load of the specimen decreases continuously. Finally, the midspan bending failure occurs.

After the eccentric compression specimen reaches the peak point, the midspan deflection deformation is more obvious. However, compared with the axial compression
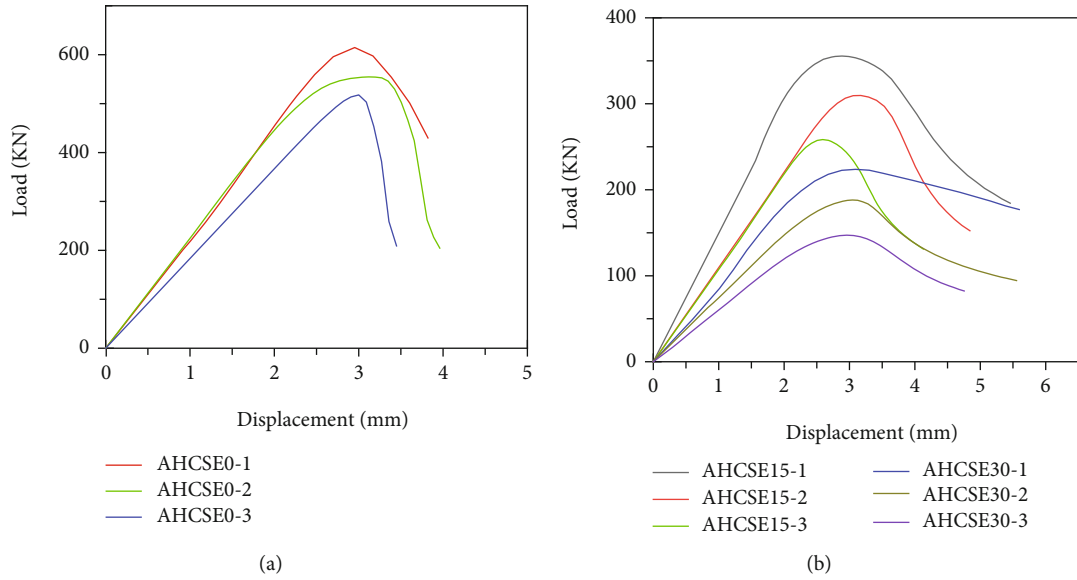
(a)

(b)

FIGURE 4: Load-displacement curve: (a) axial compression specimen; (b) eccentric compression specimen.
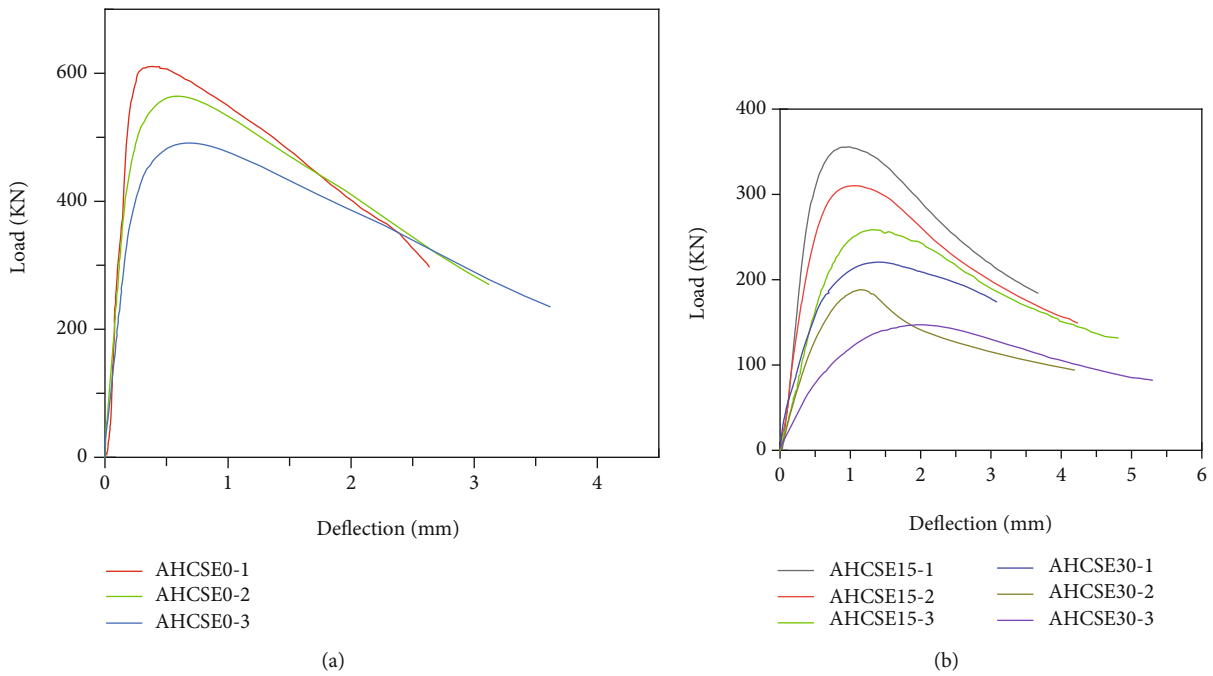

(a)

(b)

FIGURE 5: Specimen load deflection curve: (a) axial compression specimen; (b) eccentric compression specimen.

member, the greater the eccentricity of the specimen is, the slower the downward trend of the curve in the downward section is, indicating that the plastic development of the eccentric compression member is sufficient and the ductility is good. This is also consistent with the phenomenon of steel tube confined concrete members.

Overall, increasing the eccentricity of the specimen will weaken the bending stiffness and reduce the bearing capacity of the specimen, but it will increase the ductility of the specimen. Reasonable design should be made according to the needs of specimens in practical engineering.

3.4. Deflection Deformation of Typical Specimens. The lateral displacement along the column height during the whole loading process can be measured by three sets of displacement meters located at L/4, L/2, and 3L/4 positions of the specimen. Since the failure modes of the specimens are relatively consistent in the loading process, both of them are overall instability failure; two groups of typical specimens are selected as representatives for analysis in this paper. Taking the deflection deformation of the specimens as the abscissa and the height of the specimen as the ordinate, the overall lateral deflection variation diagram of the specimen
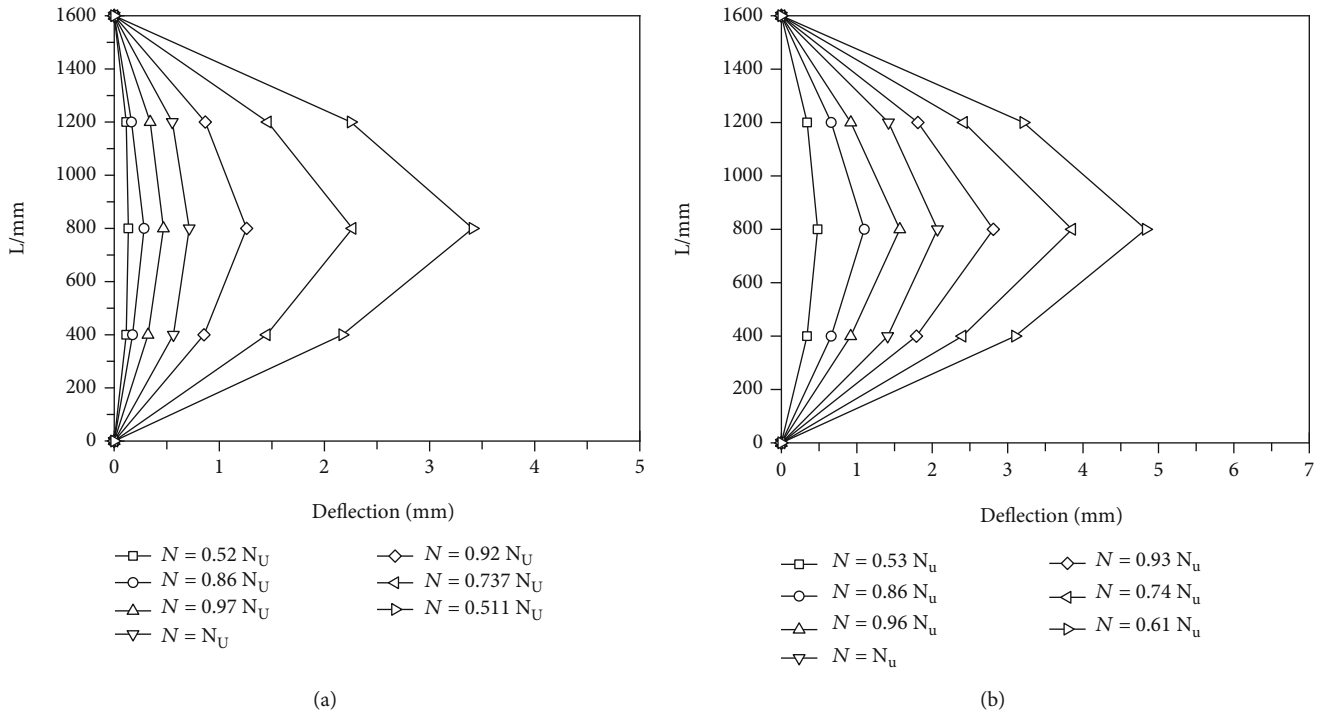
(a)

(b)

FIGURE 6: (a) 1600 mm axial compression specimen. (b)1600 mm eccentric compression specimen.

is plotted, as shown in Figure 6. N is the specimen load, and N_u is the peak load of the specimen.

It can be seen from the diagram that the change trend of the two groups of specimens is basically the same, which conforms to the sine half-wave curve. For the axial compression confined concrete column, the overall deflection at the three positions of the specimen in the elastic stage has little change, even the specimen appears reverse bending, and the deflection at both ends is slightly larger than that at the midspan. With the increase of load, the midspan deflection increases gradually when reaching the elastic-plastic stage or crossing the peak point, and the increment is greater than the deflection variation on both sides. The deflection curve gradually forms the change trend of large in the middle and small at both ends. The deflection changes of the upper and lower sides of the specimen are close, indicating that the specimen material is relatively uniform.

The deflection of eccentric compression specimen changes obviously in the elastic stage, and the deflection changes more and more when entering the elastic-plastic stage. At this time, the lateral deflection of the upper and lower positions of the specimen is slightly deviated, which may be due to the defects of the aluminum tube itself or the uneven distribution of materials during concrete pouring. With the increase of load, the deflection deformation becomes larger and larger, and the development speed of deflection is greater than that of axial compression specimen.

3.5. Load-Longitudinal Strain Curves. In order to understand the change of stress-strain of the specimen in the whole process from loading to failure, the load-strain curve is plotted

as shown in Figure 7. Since most of the specimens in this test show bending failure at the midspan position, the strain at the midspan position is the maximum. In this paper, the longitudinal strain of the compression test and the tensile test at the midspan position is taken to draw the following curve. In Figure 7, ε is the yield strain of the aluminum tube.

As shown in Figure 7(a), for the axial compression confined concrete column, the axial changes on both sides of the specimen are relatively consistent in the initial elastic stage of loading and show a linear relationship, and the change amount of longitudinal strain is relatively close, which indicates that the specimen is well aligned during installation and loading. When the load increases to about 80% of the peak load, the inflection point of the curve gradually deviates from the linear relationship and enters the elastic-plastic stage. At this time, the specimen produces deflection. The longitudinal strain of the compression side gradually increases, and the longitudinal strain of the tensile side gradually changes from the compression state to the tensile state. When the specimen reaches the peak load, the measured compressive strain of the specimen is much larger than the tensile strain and exceeds the yield strain of the aluminum tube. This shows that the material properties of the aluminum tube under pressure are fully developed. It is worth noting that with the decrease of the aspect ratio of the specimen, the strain of the tensile side aluminum tube increases gradually, which indicates that the components with small aspect ratio are more fully used for the performance of the material.

As shown in Figure 7(b), for the eccentrically loaded specimen, when the eccentricity of the specimen is small, both sides of the specimen are compressed at the same time, but the longitudinal strain of the specimen far from the
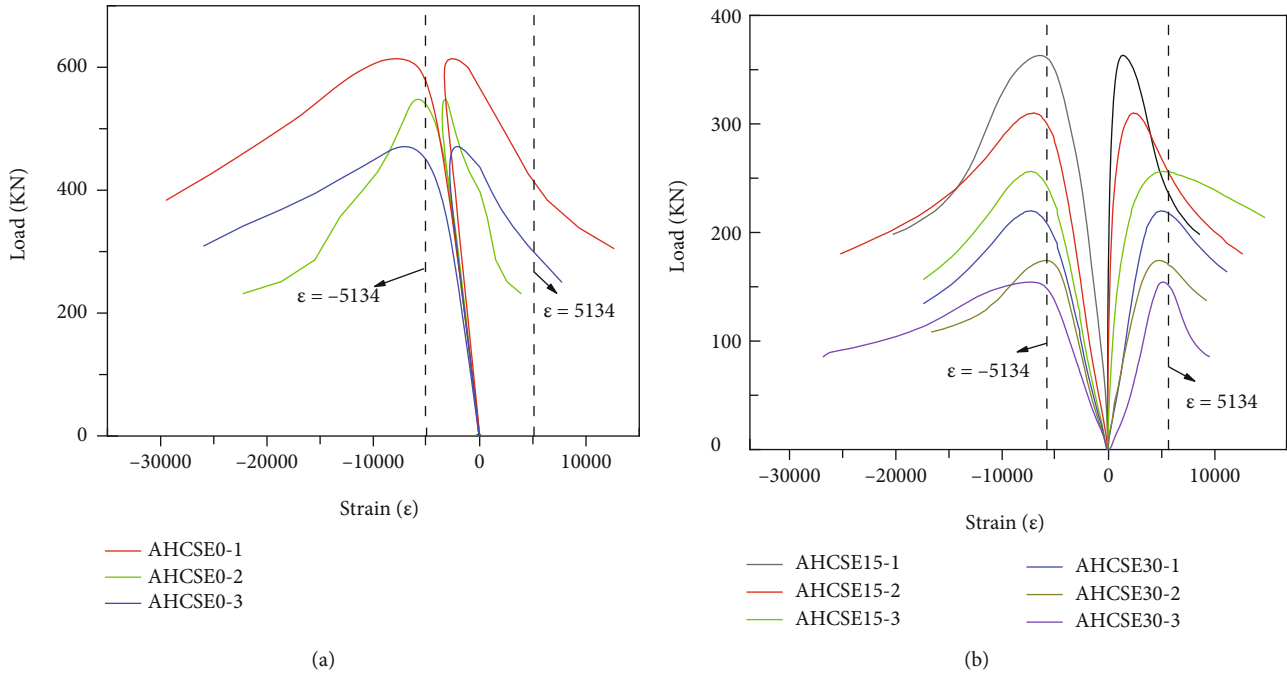
(a)

(b)

FIGURE 7: (a) Axial compression specimen. (b) Eccentric compression specimen.

eccentric position changes slowly. When the load increases to about 25%–35% of the peak load of the specimen, the specimen produces slight deflection deformation. The side far from the eccentric loading point gradually changes from the compression state to the tensile state, and the longitudinal strain of the specimen gradually changes from compression to tensile. As the load continues to increase, the specimen changes from elastic stage to elastic-plastic stage. At this time, the longitudinal strain of the compression side and the tensile side of the specimen increases sharply, but the longitudinal strain of the compression side near the eccentric loading point is still greater than the tensile test.

The longitudinal strain slope at the midspan position of the specimen with eccentricity of 30 mm is much smaller than that of the specimen with eccentricity of 15 mm. This shows that the bending stiffness of the specimen is small when the eccentricity is large. At the beginning of the loading, the specimen shows obvious compression on the tensile side of one side, and the change of the longitudinal strain on both sides of the specimen is synchronous. The longitudinal strain of the compression side is slightly larger than that of the tension side. When the specimen reaches the peak load into the descending section, the descending section of the specimen with eccentricity of 15 mm is steep, which shows that the longitudinal strain of the specimen with smaller eccentricity develops slowly and the ductility is better. This is also consistent with the phenomenon of steel tube confined concrete long column members.

3.6. Load-Circumferential Strain Curves. The circumferential strain of aluminum tube reflects the constraint of aluminum tube on concert core, which can reveal the constraint mechanism of aluminum tube on concrete under axial and eccentric compression of long column specimen. Load-cyclic

strain curves of the compression side and the tension side at the midspan of the specimen are shown in Figure 8.

Figure 8(a) shows the load-cyclic strain curves of the axially loaded specimen. At the beginning of loading, the circumferential strain of the aluminum tube is linear with the load, and the circumferential strain increments on both sides of the specimen are roughly the same. In the elastic stage, the aluminum tube and concrete are in their respective stress stages, and the aluminum tube does not form a tight hoop force on the internal concrete. At this time, the circumferential strain increment on both sides of the specimen is small. When the load reaches 75% of the peak load and enters the elastic-plastic stage, the specimen produces deflection. The strain on the compression side of the specimen increases continuously, and the circumferential strain on the tensile side changes from tension to compression. When the specimen reaches the peak load, the strain on both sides of the aluminum tube does not reach the yield strain, but the hoop strain on the compression side of the specimen is greater than that on the tension side. This indicates that the aluminum tube has produced a constraining force on the concrete at this time, and the constraining force decreases in a gradient from the compression side to the tension side.

Figure 8(b) shows the load-cyclic strain curves of the eccentrically loaded specimen. When the eccentricity of the specimen is small, the variation law of the circumferential strain and the longitudinal strain of the specimen is roughly the same, and the elastic stage shows a straight line with large slope. In the elastic-plastic stage, the circumferential strain on the tensile side of the specimen gradually changes from the tensile state to the compressive state.

When the eccentricity is large, in the initial stage of loading, the hoop strain on both sides of the specimen develops rapidly. When the load reaches the peak load, the hoop
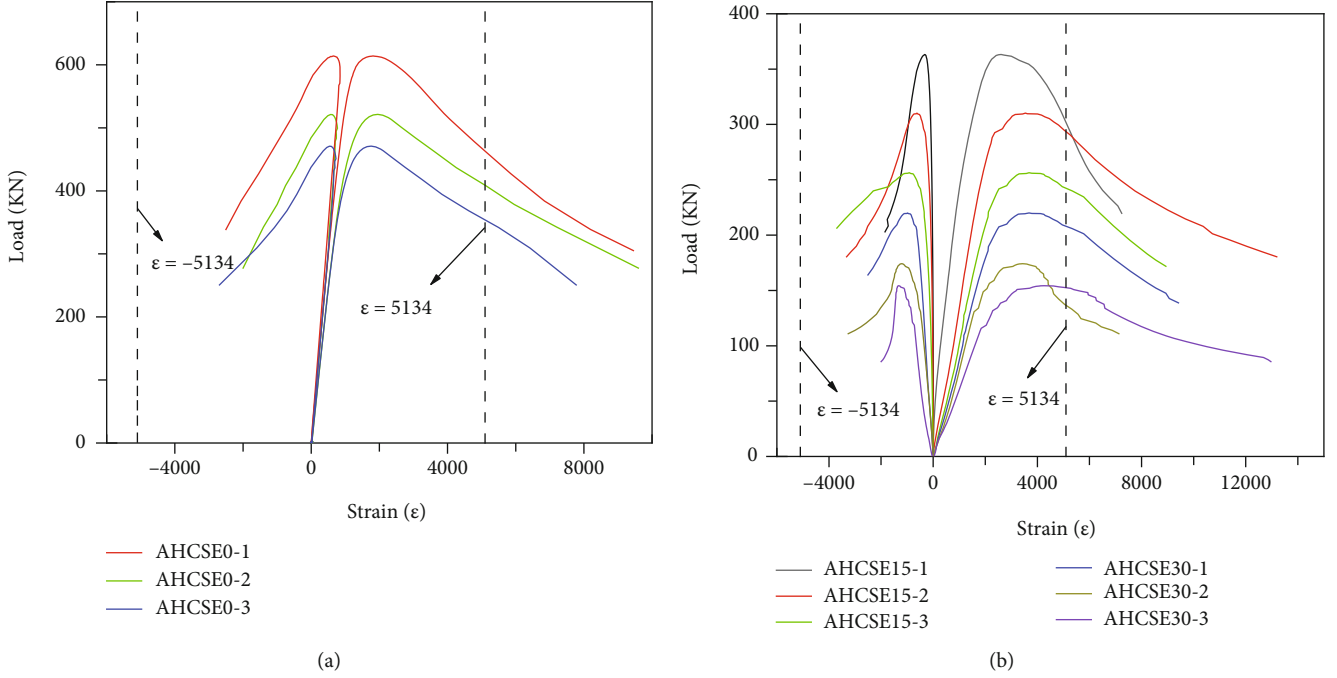
FIGURE 8: (a) Axial compression specimen. (b) Eccentric compression specimen.

strain value of the compression side is much larger than that of the tension side. The same as the coaxial compression specimen, the hoop strain of the compression side aluminum tube does not reach the yield strain when the eccentric compression specimen reaches the peak load. It is worth noting that as the aspect ratio of specimen increases, the circumferential strain of specimen also develops rapidly. This is because the components with large aspect ratio have already produced obvious deflection deformation at this time. The concrete on the compression side is crushed, and the concrete squeezes the aluminum tube in the horizontal direction. Although the aluminum tube has a restraining effect on the concrete, the specimen has obvious bending deformation at this time, and it is not suitable to continue to bear the load.

4. Finite Element Analysis

ABAQUS is a powerful commercial finite element analysis software with a variety of element libraries and material constitutive models, which has been widely used in many fields such as civil engineering and machinery. ABAQUS is one of the most popular computer-aided engineering simulation software in civil engineering. Compared with other finite element software [30, 31], ABAQUS has simple operation and clear interface. Therefore, the ABAQUS finite element software was used to simulate the 7A04 aluminum alloy tube confined concrete long column, and the experimental results are analyzed and verified.

4.1. Constitutive Model of Aluminum Alloy. Different from steel, the stress-strain curve of aluminum alloy has no obvious confined platform. The Ramberg-Osgood [32] model was adopted because it better reflects the actual properties

of aluminum alloy and has been widely recognized. The expression of the aluminum alloy is as follows:

$$\varepsilon = \frac{\sigma}{E} + \left(\frac{\sigma}{B}\right)^n, \tag{1}$$

where E is the initial elastic modulus of origin and B and n can be measured by the test.

When the residual strain is equal to 0.002, the corresponding stress is the yield strength $f_{0.2}$ that can be obtained from the following:

$$0.002 = \varepsilon - \frac{f_{0.2}}{E} = \left(\frac{f_{0.2}}{B}\right)^n. \tag{2}$$

Substitute equation (2) into equation (1)

$$\varepsilon = \frac{\sigma}{E} + 0.002 \left(\frac{\sigma}{f_{0.2}}\right)^n. \tag{3}$$

The index n is a parameter to describe strain hardening. To facilitate calculation, SteinHardt [33] proposed an approximate calculation formula in 1971. The expression is as follows:

$$10n = f_{0.2}. \tag{4}$$

4.2. Constitutive Model of Concrete. In this paper, the plastic damage model of ABAQUS is used for simulation. The plastic damage model is a damage model that describes the tension-compression isotropic and can better simulate the nonlinear behavior of concrete.

Different from the one-way force member [34, 35], the concrete core is in a complex stress state under three-

dimensional stress when the component is under compression, and the selection of concrete constitutive relationship is particularly important in ABAQUS modeling. Mander [36] model curve expression is simple, full curve, smooth, and clear theoretical concept, so this paper uses the classical Mander model simulation; the calculation formula is as follows:

$$
\begin{aligned}
\sigma &= \frac{f_{cc}xr}{r-1+x^r}, \\
x &= \frac{\varepsilon}{\varepsilon_0}, \\
r &= \frac{E_C}{E_C - E_{sec}}, \\
E_{sec} &= \frac{f_c'}{\varepsilon_0}, \\
f_c' &= 0.79 f_{cu},
\end{aligned}
\tag{5}
$$

where ε_0 is the peak strain of concrete, fc' is the peak stress of concrete, f_{cu} is the compressive strength of concrete cube, E_C is the modulus of elasticity for concrete, and E_{sec} is the concrete secant stiffness.

4.3. Finite Element Modeling. In this paper, 8-node three-dimensional simplified solid element (C3D8R) is used to model the aluminum pipe and core concrete, and the aluminum pipe and concrete are divided into regular grids, as shown in Figure 9.

The interaction between aluminum tube and concrete is defined by surface-surface contact. The aluminum tube is set as the main surface, and the core concrete is set as the slave surface. The hard contact model and the isotropic coulomb friction model are adopted along normal and tangential directions, respectively. Due to the simultaneous loading of aluminum tube and concrete, there is no or very little sliding between aluminum tube and concrete. Therefore, the friction coefficient has little effect on the structural performance of aluminum tube concrete columns. Considering that the surface of aluminum tube is smoother than that of steel tube and referring to the existing test results [37], the value of μ is 0.4.

4.4. Geometric Defects of Components. Due to the material in the production and transportation, installation process due to the existence of accidental errors will produce initial defects, especially for large slenderness component defects. Initial defects not only affect the mechanical performance of the structure but also greatly weaken the bearing capacity of the component when the defects are serious [38]. When the finite element structural analysis is carried out, the structure is usually considered as a component in an ideal state. However, the failure mode and bearing capacity of the specimen in an ideal state may be quite different from the test results.

Therefore, this paper introduces the initial geometric defects in the finite element modeling. The specimen was fully vibrated in the pouring process, and the concrete filled

with the inner wall of the aluminum tube could prevent the local buckling failure of the aluminum tube. Local instability has limited influence on the mechanical performance and bearing capacity of components, so it is not significant to analyze this defect. This paper mainly discusses the influence of initial deflection on the mechanical properties of components. The specific method is to conduct the buckling analysis of the specimen to obtain the failure mode consistent with the failure mode of the test. Then, based on the failure mode, an initial eccentricity equivalent to the defect is added to the specimen.

Buckling analysis is a method for determining the elastic critical load and buckling mode of components in ABAQUS. Buckling analysis is divided into eigenvalue buckling analysis and linear buckling analysis. Eigenvalue buckling analysis, also known as linear buckling analysis, can predict the upper limit of structural buckling load. However, due to the linear buckling analysis does not consider the geometric nonlinearity of the structure, the actual results are usually not applied to practical engineering. Therefore, nonlinear buckling analysis is usually used as a reference in finite element simulation.

Generally, L/1000 of the component is used as the initial defect of the component according to the provisions of GB 50017-2003, code for "Design of Steel Structures of China" [39] (L is the length of the component).

4.5. Verification of Short Column Finite Element Model. The finite element model established by the above constitutive model and modeling parameters is compared with the short column as the control group, as shown in Figure 10 and Table 4.

It can be observed from Figure 9 that the test curve is well fitted with the finite element curve. The ascending and descending segments of the finite element simulation curve can correctly represent the development trend of the test, and the trend of the two curves is basically the same. The peak bearing capacity ratio of three groups of specimens is between 0.977 and 0.985, and the test bearing capacity is slightly lower than the finite element calculation bearing capacity, which may be explained by the existence of accidental errors such as defects in the test. The finite element calculation of short columns is carried out in the ideal state, and the influence of defects is not considered in the short column modeling. Although the peak bearing capacity has deviation, the deviation is small within the allowable error range of the project, and the subsequent finite element simulation is based on this model.

4.6. Verification of Long Column Finite Element Model. The stress mechanism of axially loaded long columns and eccentrically loaded long columns is basically the same, and all of them are analyzed by compression-bending members. Therefore, the specimen numbered AHCSE0-15 is selected as a typical specimen for analysis. The failure mode of the specimen is shown in Figure 11.

Through the comparative analysis of test and finite element calculation, it can be seen that the failure mode of the test is basically the same as that of the finite element

(a)   (b)
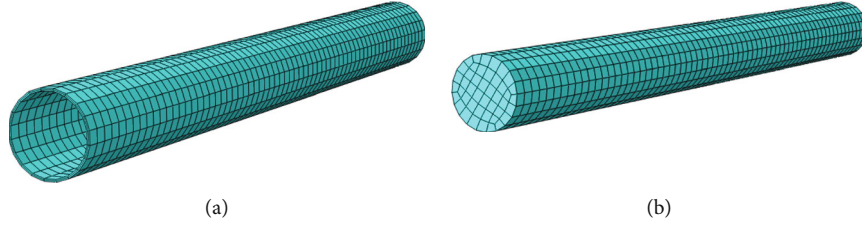
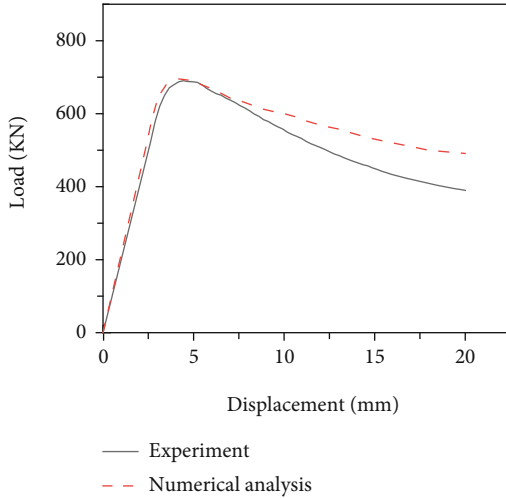FIGURE 9: (a) Grid division of aluminum tube. (b) Concrete grid division.

FIGURE 10: Numerical analysis and experimental comparison.

TABLE 4: Comparison of test values and finite element calculated values.

Specimen label	Test values N_t/kN	Simulated values N_m/kN	N_t/N_m
AHCSE0-1	692		0.985
AHCSE0-2	691	703	0.983
AHCSE0-3	687		0.977

calculation. The overall instability occurs as the bending failure of the midspan part, and the deformation curve is close to the sine half-wave curve. Since the finite element analysis was carried out in an ideal state without considering the impact and coarse aggregate subsidence caused by the aluminum tube surface during the pouring and installation of concrete, the 9 groups of long column specimens all showed bending failure at L/2 in the mid-span, which is basically consistent with the experimental phenomenon.

The comparison between the test results and the finite element load-displacement curve is presented in Figure 12. The test results agree well with the finite element simulation curve. The stiffness of the finite element simulation curve in the elastic stage is generally larger than that of the experimental curve, which may be because the finite element simulation results calculated under ideal conditions have errors with the reality. Before the beginning of the test, although some grinding and leveling work was carried out at the

end of the component, it can not guarantee the complete contact between the end face of the specimen and the hinge support. There is also a corresponding gap between the hinge support and the test instrument, resulting in some virtual displacement of the specimen during the loading process. When the curve enters the descending section, the test curve generally drops rapidly, which may be due to the rapid degradation of the stiffness of the specimen after the specimen reaches the peak bearing capacity due to the presence of defects in the loading process of the long column. Although the influence of defects is considered in the finite element modeling, the inhomogeneity of concrete and small defects on the surface of aluminum tube cannot be restored in the test. Nevertheless, the finite element simulation curve can correctly describe the actual development trend of the test curve.

The ultimate bearing capacity of the axial and eccentric compression specimens of 9 groups of long column specimens was compared with the simulated data. As shown in Table 5, the ratio of test ultimate load to simulate ultimate load is 0.94-1.07, and the ratio error is within 10%, which is within the allowable range of engineering error. This also shows that the ABAQUS modeling method used in this paper is feasible.

5. Bearing Capacity Calculation

5.1. Calculation of Short Column Bearing Capacity. Before calculating the bearing capacity of 7A04 aluminum alloy tube concrete long columns, it is necessary to determine the calculation formula of the ultimate bearing capacity of short columns. Based on the existing extensive research on the mechanical properties of 7A04 aluminum alloy tube concrete short columns by our research group [40], this paper obtains the calculation formula of the bearing capacity of 7A04 aluminum alloy tube concrete short column:

$$N_u = \gamma_c A_c f_c' + \gamma_{AL}(1 + \eta)A_s f_y, \tag{6}$$

where f_c' is the compressive strength of concrete cylinder, γ_c is the compressive strength reduction coefficient of concrete cylinder (0.85), η is the steel tube strength improvement coefficient (0.27), and γ_{AL} is the strength reduction coefficient of aluminum alloy tube (0.8) and where γ_c, η, and γ_{AL} are taken as 0.85, 0.27, and 0.8.

The bearing capacity of short columns obtained in the above section is compared with the calculation formula of

(a)   (b)

Figure 11: (a) Test failure mode. (b) Numerical analysis of failure mode.

bearing capacity, and the results are shown in Table 6. The theoretical value calculated by the formula is slightly less than the experimental value, which indicates that the theoretical value is conservative and feasible. On the whole, the two results are relatively close, and the relative error is small. The subsequent calculation of axial compression and eccentric compression bearing capacity of 7A04 aluminum alloy tube concrete long column is based on the bearing capacity calculation formula of this short column.

5.2. Calculation of Bearing Capacity of Long Column under Axial Compression. Due to the bending instability failure of long column members, the elastic modulus of aluminum alloy is lower than that of steel, so the bending stiffness of aluminum alloy filled concrete member is lower than that of steel tube filled concrete member, and the bearing capacity of aluminum tube filled concrete member is also lower. Therefore, it is necessary to discuss the bearing capacity of long column members filled with aluminum tube concrete.
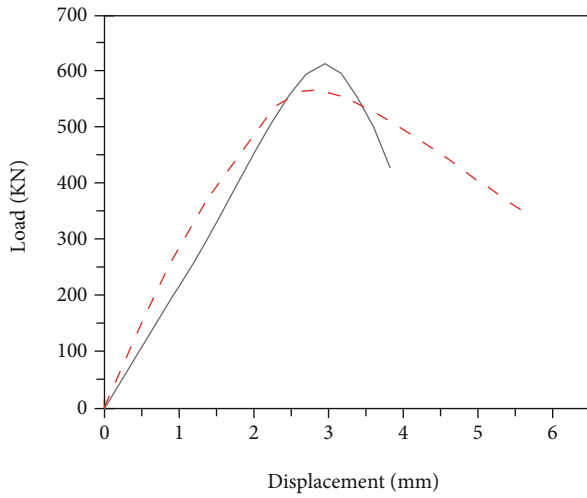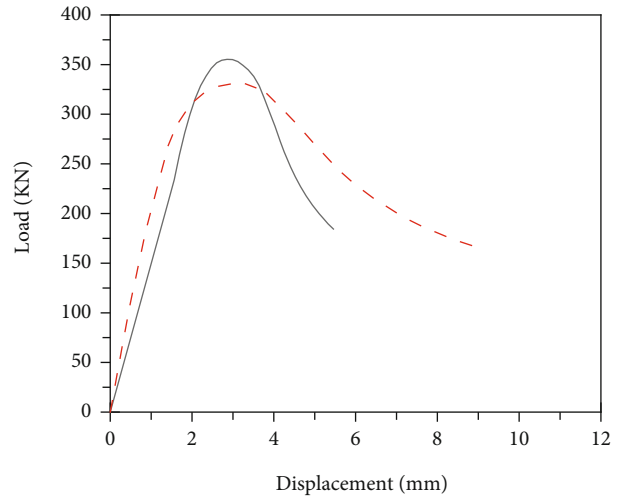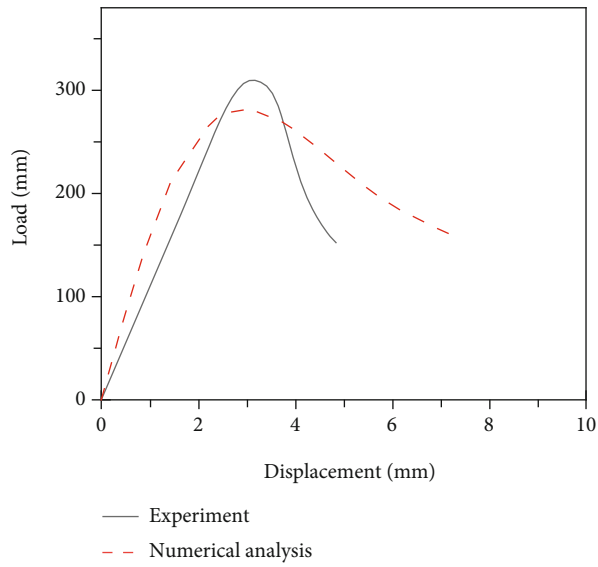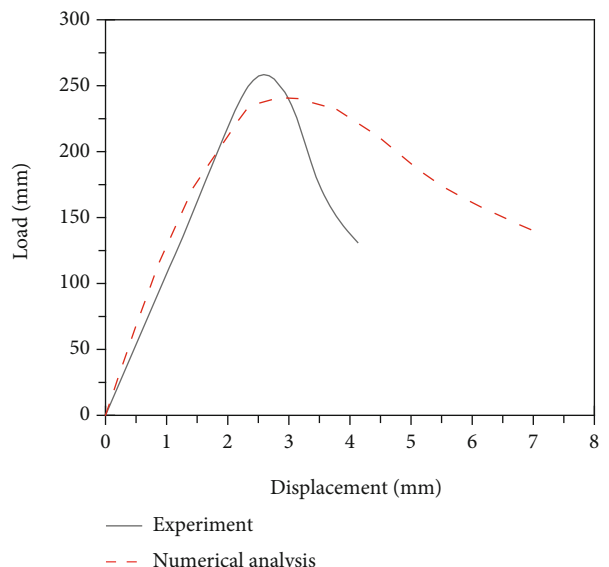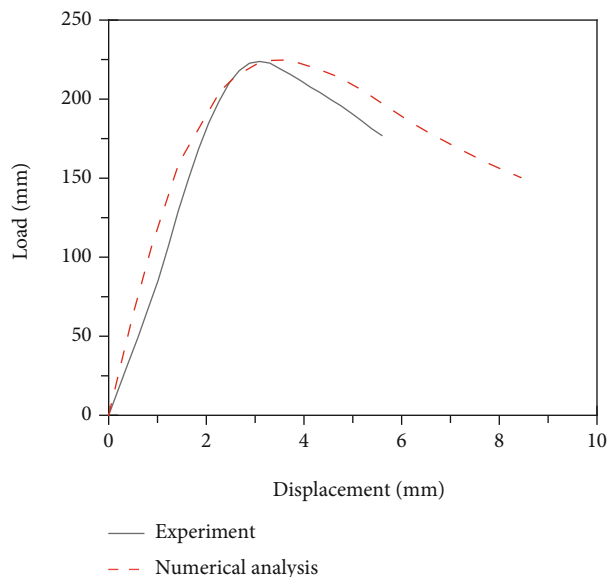
(a)
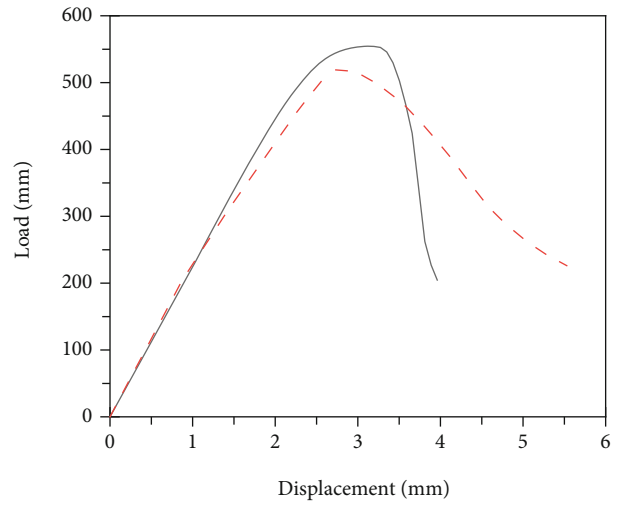
(b)
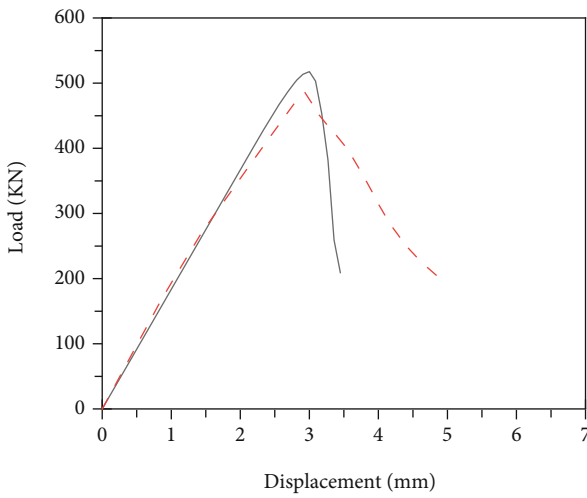
(c)

(d)

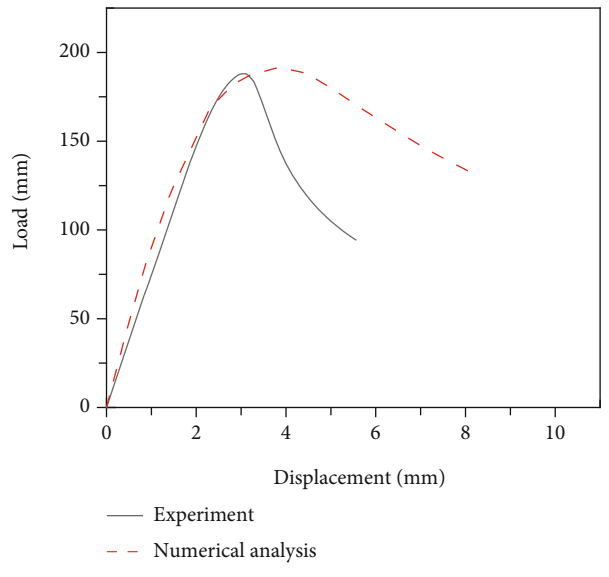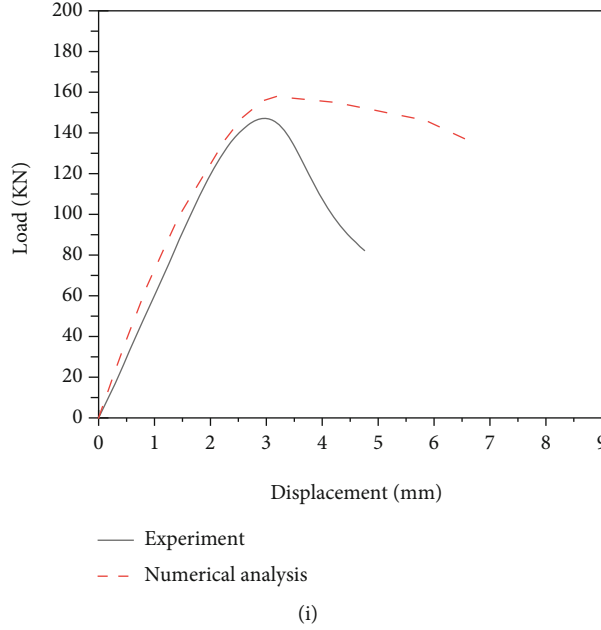Figure 12: Continued.

(e)

(f)

(g)

(h)

Figure 12: Continued.

(i)

FIGURE 12: Specimen load-displacement curve: (a)AHCSE0-1; (b)AHCSE0-2; (c) AHCSE0-3; (d) AHCSE15-1; (e) AHCSE15-2; (f) AHCSE15-3; (g) AHCSE30-1; (h) AHCSE30-2; (i) AHCSE30-3.

TABLE 5: Comparison of test values and finite element calculated values.

Specimen label	Test values N_t/kN	Simulated values N_m/kN	N_t/N_m
AHCSE0-1	598	568	1.05
AHCSE0-2	540	511	1.06
AHCSE0-3	470	467	1.01
AHCSE15-1	363	338	1.07
AHCSE15-2	311	289	1.07
AHCSE15-3	257	241	1.07
AHCSE30-1	220	224	0.98
AHCSE30-2	182	191	0.95
AHCSE30-3	154	158	0.98

TABLE 6: Comparison of test values and theoretical formula calculation values.

Specimen label	Test values N_t/kN	Formula calculated values N_u/kN	N_t/N_u
AHCSE0-1	692		1.01
AHCSE0-2	691	687	1.01
AHCSE0-3	687		1

At present, the calculation of axial compression confined concrete columns of long column members at home and abroad is mostly calculated by multiplying the ultimate bearing capacity of short columns by a stability coefficient (ϕ_l). Where $N_c = N_u\phi_l$, N_u is the ultimate bearing capacity of the short column. N_c is the ultimate bearing capacity of the long column specimen. This paper uses formula (6) to calculate N_u.

In the specification [26], various defects such as initial bending, initial eccentricity, and residual stress are equivalent to a coefficient related to the slenderness ratio. However, the specification only specifies the calculation of the stability factor for 5 series and 6 series aluminum alloys. 7A04 aluminum alloy has high strength, which can not only give full play to the advantages of high strength aluminum pipes to increase its restraint effect on the core concrete but also improve the overall stability of the components. Considering the influence of 7A04 aluminum alloy on the improvement of the overall stability of the long column specimen, it is necessary to reduce the defect coefficient of the specimen. This subsection refers to the specification [26] for the calculation form of the stability coefficient, take the regularized slenderness ratio of the specimen (obtained by dividing the slenderness ratio by the radius of gyration of the specimen) as the abscissa and the stability coefficient as the ordinate (obtained by dividing the bearing capacity of the axial compression specimen by the axial compression bearing capacity of the short column). Through the regression analysis of nine groups of simulation data and three groups of experimental data, Figure 13 shows the fitting results of regular slenderness ratio calculated and stability coefficient obtained by experiment and simulation.

That is, the expression of the stability coefficient of the axial compression member is as follows:

$$\phi_l = \frac{1 + \eta' + \lambda^2}{2\lambda^2} - \sqrt{\left(\frac{1 + \eta' + \lambda^2}{2\lambda^2}\right) - \frac{1}{\lambda^2}}. \quad (7)$$
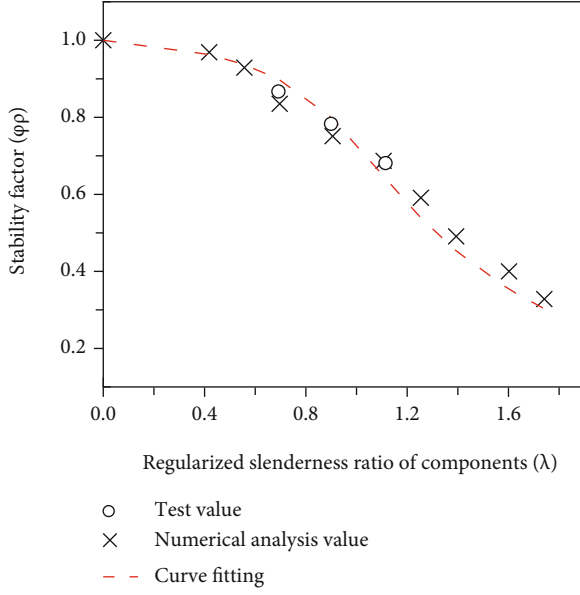
FIGURE 13: Relationship between regular slenderness ratio and stability coefficient.
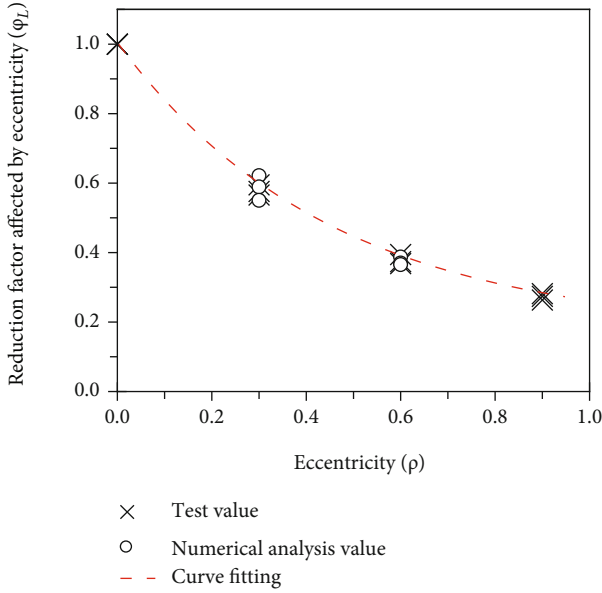

FIGURE 14: The relationship between eccentricity and bearing capacity reduction.

$\bar{\lambda}$ is the member slenderness ratio ($L/\sqrt{I_a/A_a}$), where I_a is the moment of inertia of aluminum tube and A_a is the aluminum tube cross-sectional area. λ is the regular slenderness ratio of components shown as follows:

$$\lambda = \frac{\bar{\lambda}}{\pi} \sqrt{\frac{f_{0.2}}{E_a}}. \qquad (8)$$

η is the member geometric defect factor. The following is for weakly hardening alloys: $\alpha = 0.2$, $\bar{\lambda}_0 = 0.15$. The follow-

TABLE 7: Comparison of bearing capacity reduction factor calculated under axial compression with test and formula calculation values.

Serial number	L/D	f_{ck} (MPa)	f_y (MPa)	ϕ_L	ϕ'_L	ϕ_L/ϕ'_L
1	10	45.41	400	0.867	0.899	0.964
2	13	45.41	400	0.783	0.800	0.979
3	16	45.41	400	0.681	0.647	1.053
4	6	40.13	400	0.969	0.963	1.006
5	8	40.13	400	0.929	0.937	0.992
6	10	40.13	400	0.835	0.897	0.931
7	13	40.13	400	0.751	0.796	0.944
8	16	40.13	400	0.687	0.641	1.071
9	18	40.13	400	0.591	0.539	1.097
10	20	40.13	400	0.491	0.453	1.085
11	23	40.13	400	0.400	0.353	1.133
12	25	40.13	400	0.328	0.303	1.083
Mean value						1.028
Standard deviation						0.064
Coefficient of variation						0.062

$^*\varphi_L$ is the bearing capacity reduction factor obtained from the test, φ'_L is the reduction coefficient of bearing capacity calculated by the formula, and f_{ck} is the axial compression strength of concrete.

ing is for strong hardening alloys: $\alpha = 0.35$, $\bar{\lambda}_0 = 0.1$. η_0 is the defect reduction factor (0.6). η' is the corrected defect factor; $\eta' = \eta_0 \eta$.

5.3. Calculation of Eccentric Compression Bearing Capacity of Long Columns. The stable bearing capacity of the eccentrically compressed specimen can be obtained by multiplying the bearing capacity reduction factor affected by the eccentricity on the basis of the axial compression of the long column [20–22].

Based on the test and finite element simulation in the previous section, the influence of eccentricity $\rho(0.3, 0.6, 0.9)$ on the bearing capacity reduction of long columns with slenderness ratios $\lambda(40, 52, 64)$ was investigated. Through regression analysis of 6 sets of test data and 9 sets of simulated data (Figure 14), the bearing capacity reduction formula of the biased long column affected by the eccentricity is obtained. The abscissa is the eccentricity of the specimen obtained by dividing the eccentricity by the section radius; the ordinate is the bearing capacity reduction factor affected by the eccentricity obtained by dividing the bearing capacity of the eccentric compression specimen with the same aspect ratio by the bearing capacity of the axial compression specimen.

That is, the expression of the bearing capacity reduction factor of the biasing member is as follows:

$$\phi = 0.17 + 0.829 \exp\left(-\frac{\rho}{0.453}\right). \qquad (9)$$

TABLE 8: Comparison of eccentric compression calculation bearing capacity reduction coefficient with test and formula calculation values.

Serial number	L/D	Eccentricityρ	f_{ck} (MPa)	f_y (MPa)	ϕ_ρ	ϕ'_ρ	ϕ_ρ/ϕ'_ρ
1	10	0.3	45.41	400	0.595	0.597	0.996
2	10	0.6	45.41	400	0.394	0.391	1.007
3	10	0.9	40.13	400	0.281	0.283	0.992
4	13	0.3	45.41	400	0.565	0.597	0.946
5	13	0.6	45.41	400	0.373	0.391	0.953
6	13	0.9	40.13	400	0.273	0.283	0.964
7	16	0.3	45.41	400	0.556	0.597	0.931
8	16	0.6	45.41	400	0.338	0.391	0.8644
9	16	0.9	40.13	400	0.263	0.283	0.929
Mean value							0.954
Standard deviation							0.041
Coefficient of variation							0.043

*φ_ρ is the bearing capacity reduction factor obtained from the test, and φ'_ρ is the reduction coefficient of bearing capacity calculated by the formula.

TABLE 9: Comparison of test values and theoretical formula calculation values.

Specimen label	Test values N_t/kN	Formula calculated values N_c/kN	N_t/N_c
AHCSE0-1	598	617	0.968
AHCSE0-2	540	549	0.982
AHCSE0-3	470	444	1.057
AHCSE15-1	363	368	0.984
AHCSE15-2	311	328	0.947
AHCSE15-3	257	265	0.968
AHCSE30-1	220	241	0.911
AHCSE30-2	182	214	0.846
AHCSE30-3	154	173	0.941

*N_L is the calculated value of the theoretical formula.

5.4. *Verification of Calculation Formula of Bearing Capacity.* The theoretical calculation formula of the above correction is verified, and the corrected theoretical calculation value is compared with the experimental value and the simulation value. The corresponding results are shown in Tables 7–9.

By comparing the experimental and simulated data in Tables 7 and 8 with the formula proposed in this paper, it is found that the theoretical calculation formula of axial compression has an average value of 1.028, a standard deviation of 0.064, and a coefficient of variation of 0.062. The theoretical calculation formula of eccentric compression is 0.062. The mean value of the calculation formula is 0.954, the standard deviation is 0.041, the coefficient of variation is 0.043, and the error is within 15%, which meets the need of practical engineering. As shown in Table 9, the ratio of the experimental value to the calculated value of the theoretical formula is less than 15%. Therefore, the calculation formula of the bearing capacity of the 7A04 aluminum alloy tube concrete long column can be obtained by the formula suggested in this paper. The revised theoretical calculation formula proposed in this paper has a clear theoretical concept and clear meaning, which is basically consistent with the current international mainstream method for calculating the stability coefficient of long columns, and can be used as a useful supplement for calculating the bearing capacity of 7A04 aluminum alloy tube concrete long columns.

The formula for calculating the bearing capacity of 7A04 aluminum alloy tubular concrete long column is as follows:

$$N_c = N_u \phi_L \phi_\rho, \tag{10}$$

where N_u is the ultimate bearing capacity of short column and ϕ_L is the reduction factor considering slenderness ratio to bearing capacity of members and ϕ_ρ considering the reduction factor of eccentricity to bearing capacity of members.

6. Conclusion

In this paper, experimental exploration and finite element analysis of 7A04 aluminum alloy tube confined high strength concrete long columns are carried out. The conclusions are as follows:

(1) The bearing capacity of specimens decreases with the increase of aspect ratio and eccentricity, but it is more obvious affected by eccentricity. When the load of the axial compression specimen is close to the peak value or reaches the peak value, a slight deflection deformation of the specimen can be observed; When the load of eccentrically loaded specimen reaches 70% of its maximum bearing capacity. It can be observed that obvious deflection deformation has occurred in the midspan of the specimen. This also shows that the eccentric compression confined concrete column reaches the elastic critical point faster than the axial compression confined concrete column

(2) When the axial compression specimen starts to be loaded, the specimen is compressed along the entire section in the longitudinal direction. When it reaches the elastic-plastic stage, the midspan of the specimen changes from compression on both sides to tension on one side and compression on one side. Due to the small bending stiffness of the eccentric compression specimen, the specimen undergoes slight deflection deformation at the initial stage of loading, which is manifested as obvious compression on one side and tension on the other side. The stiffness and bearing capacity of the specimen decreased with the increase of eccentricity, but the ductility increased

(3) The trend of the load-displacement curves of the axial compression specimen and the eccentric compression specimen is roughly the same, and the slope of the axial compression specimen is generally larger than that of the eccentric compression specimen in the elastic stage; it is proposed to calculate the length of the 7A04 aluminum alloy concrete tube. The calculation formula of the bearing capacity of the column and the theoretical formula fit well with the experimental and simulated values and can be used as a reference for evaluating the bearing capacity of the long column of 7A04 aluminum alloy tube concrete

Data Availability

The data are generated from experiments and can be available from the corresponding author upon request. Their financial support is highly appreciated.

Conflicts of Interest

The authors declare that there are no conflicts of interest regarding the publication of this paper.

Acknowledgments

References

[1] L.-H. Han, W. Li, and R. Bjorhovde, "Developments and advanced applications of concrete-filled steel tubular (CFST) structures: members," *Journal of Constructional Steel Research*, vol. 100, pp. 211–228, 2014.

[2] J. Ma, X. L. Li, J. G. Wang et al., "Experimental study on vibration reduction technology of hole-by-hole presplitting blasting," *Geofluids*, vol. 2021, 10 pages, 2021.

[3] J. Wang, T. Zuo, X. Li, Z. Tao, and J. Ma, "Study on the fractal characteristics of the pomegranate biotite schist under impact loading," *Geofluids*, vol. 2021, 8 pages, 2021.

[4] X. L. Li, S. J. Chen, Z. H. Li, and E. Y. Wang, "Rockburst mechanism in coal rock with structural surface and the microseismic (MS) and electromagnetic radiation (EMR) response," *Engineering Failure Analysis*, vol. 124, no. 6, article 105396, 2021.

[5] N. E. Shanmugam and B. Lakshmi, "State of the art report on steel-concrete composite columns," *Journal of Constructional Steel Research*, vol. 57, no. 10, pp. 1041–1080, 2001.

[6] L. H. Han, G. H. Yao, and Z. Tao, "Performance of concrete-filled thin-walled steel tubes under pure torsion," *Thin-Walled Structures*, vol. 45, no. 1, pp. 24–36, 2007.

[7] Z. Tao, L.-H. Han, and D.-Y. Wang, "Strength and ductility of stiffened thin-walled hollow steel structural stub columns filled with concrete," *Thin-Walled Structures*, vol. 46, no. 10, pp. 1113–1128, 2008.

[8] E. Ellobody, B. Young, and D. Lam, "Behaviour of normal and high strength concrete-filled compact steel tube circular stub columns," *Journal of Constructional Steel Research*, vol. 62, no. 7, pp. 706–715, 2006.

[9] H. Hsuan-Teh, C.-S. Huang, M.-H. Wu, and Y.-M. Wu, "Nonlinear analysis of axially loaded concrete-filled tube columns with confinement effect," *Journal of Structural Engineering*, vol. 129, no. 10, pp. 1322–1329, 2003.

[10] S. M. Liu, X. L. Li, D. K. Wang, and D. Zhang, "Experimental study on temperature response of different ranks of coal to liquid nitrogen soaking," *Natural Resources Research.*, vol. 30, no. 2, pp. 1467–1480, 2021.

[11] X. G. Kong, D. He, X. F. Liu et al., "Strain characteristics and energy dissipation laws of gas-bearing coal during impact fracture process," *Energy*, vol. 242, article 123028, 2022.

[12] X. G. Kong, S. G. Li, E. Y. Wang et al., "Experimental and numerical investigations on dynamic mechanical responses and failure process of gas-bearing coal under impact load," *Soil Dynamics and Earthquake Engineering*, vol. 142, article 106579, 2021.

[13] Y. Niu, E. Wang, Z. Li et al., "Identification of coal and gas outburst-hazardous zones by electric potential inversion during mining process in deep coal seam," *Rock Mechanics and Rock Engineering*, vol. 85, 2022.

[14] R. L. Temlin, R. G. Strum, E. C. Hartman et al., *Column Strengh of Various Aluminum Alloys*, Alcoa Technical Paper, Pittsburgh, 1938.

[15] M. Holt, "Tests on built-up columns of structural aluminum alloys," *Transactions of the American Society of Civil Engineers*, vol. 105, no. 1, pp. 196–217, 1940.

[16] J. W. Clark and R. L. Rolf, "Design of aluminum tubular members," *Journal of the Structural Division*, vol. 90, no. 6, pp. 259–289, 1964.

[17] H. N. Hill, "Design of welded aluminum structures," *ASCE*, vol. 127, no. 2, pp. 102–126, 1962.

[18] C. Faella and F. M. Mazzolani, "Simulation of the behavior of inelastic industrial bars under axial load," *Construction Metal*, vol. 4, 1974.

[19] G. Valtinat and R. Muller, *Alu-Alloy Welded Column Buckling Research Program: Numerical Computations*, ECCS Committee, 1976.

[20] F. F. Buckling, *Lateral Buckling and Eccentric Buckling of Aluminum Alloy Columns, Beams, and Bean-Columns*, ECCS Committee, 1977.

[21] F. M. Mazzolani, *Aluminum Alloy Structures*, Chapman & Hall, london, 2nd ed edition, 1994.

[22] L. Yongfeng, J. Yue, R. Yuan, and C. Yangji, "Study on stability of axial compression rods for aluminum alloy structures," *Journal of Tongji University*, vol. 29, no. 4, pp. 401–405, 2001.

[23] Z. Zheng, *Study on Stability Capacity of Aluminum Alloy Structures*, Tongji University, Shanghai, 2006.

[24] S. Guo, S. Li, S. Qiu Yuanqi, Q. Z. Ci, and Y. Nianliang, "Research on constitutive relationship and physical and mechanical properties of aluminum alloy materials for domestic structures," *Journal of Building Structures*, vol. 28, no. 6, pp. 110–117, 2007.

[25] H. Riqin, *Study on the Stability Bearing Capacity of Angular High-Strength Aluminum Alloy Members under Axial Compression*, Harbin Institute of Technology, Harbin, 2013.

[26] National standard of the People ' s Republic of China, *GB 50429-2007, Aluminum Alloy Structure Design Specification*, China Standard Press, Beijing, 2007.

[27] G. H. Xing and O. E. Ozbullut, "Flexural performance of concrete beams reinforced with aluminum alloy bars," *Engineering Structures*, vol. 126, pp. 53–65, 2016.

[28] Z. Zhongming and L. Wei, *Technical Specification for Concrete-Filled Steel Tube Structures: GB50936 – 2014*, China Construction Industry Press, Beijing, 2014.

[29] Ministry of Housing and Urban-Rural Development of the People 's Republic of China, *Standard for Test Methods of Concrete Structures GB/T 50152*, China Construction Industry Press, Beijing, 2012.

[30] X. L. Li, S. J. Chen, Q. M. Zhang, X. Gao, and F. Feng, "Research on theory, simulation and measurement of stress behavior under regenerated roof condition," *Geomechanics and Engineering*, vol. 26, no. 1, pp. 49–61, 2021.

[31] W. Shen, S. Guocang, Y. Wang, B. Jianbiao, Z. Ruifeng, and X. Wang, "Tomography of the dynamic stress coefficient for stress wave prediction in sedimentary rock layer under the mining additional stress," *International Journal of Mining Science and Technology*, vol. 31, no. 4, pp. 653–663, 2021.

[32] W. Ramberg and W. R. Osgood, *Description of Stress-Straincurves by Three Parameters*, NACATN-902, Washington DC, 1943.

[33] O. SteinHardt, "Aluminum constructions in civil engineering," *Aluminum*, vol. 47, pp. 131–139, 1971.

[34] X. L. Li, S. J. Chen, S. M. Liu, and Z. H. Li, "AE waveform characteristics of rock mass under uniaxial loading based on Hilbert-Huang transform," *Journal of Central South University*, vol. 28, no. 6, pp. 1843–1856, 2021.

[35] Z. Li, X. Zhang, Y. Wei, and M. Ali, "Experimental study of electric potential response characteristics of different lithological samples subject to uniaxial loading," *Rock Mechanics and Rock Engineering*, vol. 54, no. 1, pp. 397–408, 2021.

[36] J. B. Mander, M. J. N. Priestley, and R. Park, "Theoretical stress-strain model for confined concrete," *Journal of Structural Engineering*, vol. 114, no. 8, pp. 1804–1826, 1988.

[37] Z. Xiang, W. Wan-bo, H. Jing-si, and H. Tao, "Study on axial compression bearing capacity of circular aluminum alloy tube concrete short columns," *Engineering Mechanics*, vol. 38, no. 2, pp. 52–60, 2021.

[38] C. Lyu, J. Liu, Y. Ren, C. Liang, and Y. Liao, "Study on very long-term creep tests and nonlinear creep-damage constitutive model of salt rock," *International Journal of Rock Mechanics and Mining Sciences*, vol. 146, 2021.

[39] GB 50017—2003, *Code for Design of Steel Structures*, China Planning Press, Beijing, 2003.

[40] L. Pengju, *Axial Compressive Experimental Study of 7A04 Aluminum Alloy Round Tube High-Strength Concrete Short Column*, Xinjiang University, Xinjiang, 2021.